Modeling and experimental observation of an on-chip two-dimensional far-field interference pattern

Amir Hosseini,[1,2,*] David Kwong,[1,2] Yang Zhang,[1,2] Andrea Alu,[1] and Ray T. Chen[1,2]

[1]Department of Electrical and Computer Engineering, University of Texas at Austin, 1 University Street, Austin, Texas 78712, USA

[2]Miroelectronic Research Center, University of Texas at Austin, 10100 Burnet Road, Austin, Texas 78758, USA

*Corresponding author: ahoss@mail.utexas.edu

Received 2 November 2010; revised 9 February 2011; accepted 27 February 2011; posted 2 March 2011 (Doc. ID 137553); published 20 April 2011

In this paper, we model and experimentally observe the far-field radiation produced by interfering beams propagating in two-dimensional (2D) slab waveguides. Using a transmission-line analogy, we compare the 2D propagation with standard three-dimensional (3D) far-field representations and derive the 2D conditions for using standard far-field approximations. Then we test our theoretical results by experimentally observing the 2D far-field pattern produced by a 1 × 3 multimode interference (MMI) coupler on a silicon nanomembrane. The MMI outputs are connected to a slab silicon waveguide, and the far field is observed at the edge of the silicon slab. This represents the observation of 2D far-field pattern produced by an array of on-chip radiators. © 2011 Optical Society of America

OCIS codes: 130.2790, 130.3120, 070.2580.

1. Introduction

On-chip optical phased arrays (OPAs) that may provide optical beam steering have been used to realize fast (18 GHz) optical switches [1]. In such systems, an input optical beam is split into several arms and properly phase shifted. The output waveguides of the OPA are connected to a slab waveguide in which the field propagates freely in two dimensions and is confined in the direction perpendicular to the array's plane. These setups may be a first step toward OPAs in free space, when properly combined with optical antennas, in order to control the near- and far-field radiation on chip.

In this paper, we model field propagation generated by an array of point sources confined in a silicon slab waveguide. The silicon slab thickness is chosen to be small enough for single-mode operation. We derive far-field conditions for such 2D radiation in order to use simple array factors to determine the on-chip radiation from the OPAs. Finally, we fabricate an on-chip three-element OPA and present an experimental setup to observe the 2D far-field pattern. Using a 1 × 3 multimode interference (MMI) coupler, we feed the array elements with uniform power while creating a phase shift in the array. Then we compare the observed far-field interference pattern with the theoretical calculations. We show that the observation plane is in fact in the far-field zone. Therefore, this is the first observation of a 2D optical far-field interference pattern.

Although we investigate 2D propagation in a silicon nanomembrane slab waveguide, the results of this study can be used for problems that involve free propagation in 2D and confinement in the third direction such as in Ref. [2], in which a surface plasmon polariton (SPP) wave propagation at the surface of a metallic film is studied. Note that due to the high loss of the SPP waves and the low sensitivity of the measurement setups, the interference pattern was observed in the middle zone, as opposed to the far-field zone. The presented work here may be interpreted as an application of the theory of Flatland Optics [3], together with the demonstration of an optical setup to observe and measure the 2D far-field

0003-6935/11/131822-05$15.00/0
© 2011 Optical Society of America

patterns and a comparison between theoretical calculations and measurements. There have been experimental efforts aimed to confirm the concept of Flatland Optics [4,5]. However, to the best of our knowledge, this is the first observation of 2D optical far-field on-chip radiation and interference.

2. Two-Dimensional Far-Field Formulation

In this section, we model the field radiated by a point source or an array of point sources in a slab dielectric waveguide. The vertically symmetric structure shown in Fig. 1 is well known to support the transverse electric (TE, $E_x = E_z = H_y = 0$) mode without a cutoff thickness. We assume that the slab thickness is small enough to allow only single-mode operation in the z direction. We focus here on TE-polarized propagation, assuming that a point source excites this slab waveguide with the field distribution $E_y = f(z)\delta(x)\delta(y)$, where $f(z)$ is the field distribution along z, given as

$$f(z) = \begin{cases} A\cos(\beta_z h)\exp[-\alpha(z-h)] & z > h \\ A\cos(\beta_z z) & |z| \le h \\ A\cos(\beta_z h)\exp[\alpha(z+h)] & z < -h \end{cases},$$

with the well known dispersion relation:

$$\left(h\sqrt{\varepsilon\mu\omega^2 - \beta_\rho^2}\right)\tan\left(h\sqrt{\varepsilon\mu\omega^2 - \beta_\rho^2}\right) = -ih\sqrt{\varepsilon_c\mu\omega^2 - \beta_\rho^2}, \quad \text{where} \quad \beta_\rho^2 = \beta_x^2 + \beta_y^2,$$

$\alpha = -i(\varepsilon_c\mu\omega^2 - \beta_\rho^2)^{1/2}$. In order to calculate the field emitted by such a point source in the slab, we notice that a TE ($E_x = E_z = H_y = 0$)-polarized line source along the y axis in the form of $E_y = f(z)\exp(-j\beta_y y)\delta(x)$ excites the TE-polarized modes with the electric field:

$$E_y = \frac{j}{2\beta_x} f(z)\exp(-j\beta_y y)\exp(-j\beta_x x). \tag{1}$$

Since $\delta(x)\delta(y) = \frac{\delta(x)}{2\pi}\int_{-\infty}^{\infty}\exp(-j\beta_y y)\mathrm{d}\beta_y$, the field emitted by a point source in the slab may be written, due to linearity, as the superposition of modes excited by line sources with dependence in the form of $\exp(-j\beta_y y)$:

$$E_y = \int_{-\infty}^{\infty}\frac{j}{4\pi\beta_x} f(z)\exp(-j\beta_x x)\exp(-j\beta_y y)\mathrm{d}\beta_y. \tag{2}$$

In order to calculate this integral, we notice that

$$H_0^{(2)}(\beta_\rho\rho,\varphi) = \frac{1}{\pi}\int_{\pi/2-j\infty}^{3\pi/2+j\infty}\exp[j\beta_\rho\rho\cos(\zeta-\varphi)]\mathrm{d}\zeta, \tag{3}$$

where (ρ,φ,z) is the cylindrical coordination [6]. Using Eq. (3), one can show that [Appendix A]

$$\int_{-\infty}^{\infty}\frac{1}{\beta_x}\exp(-j\beta_x x)\exp(-j\beta_y y)\mathrm{d}\beta_y = \pi H_0^{(2)}(\beta_\rho\rho). \tag{4}$$

Therefore, a point source given as $E_y = f(z)\delta(x)\delta(y)$ generates a propagating field in the slab as follows:

$$E_y = \int_{-\infty}^{\infty}\frac{j}{4\pi\beta_x} f(z)\exp(-j\beta_x x)\exp(-j\beta_y y)\mathrm{d}\beta_y = \frac{j}{4} f(z)H_0^{(2)}(\beta_\rho\rho). \tag{5}$$

As expected, this result coincides with the 2D Green's function $G(x,y) = \frac{j}{4}H_0^{(2)}(k\sqrt{x^2+y^2})$ solution to the Helmholtz equation $\nabla^2 G + k^2 G = \delta(x,y)$.

Our goal is to obtain the far-field radiation from an array of line sources arbitrarily located along the y axis. In the far field, we can write [7]

$$H_0^{(2)}(\beta_\rho\rho) \approx \sqrt{\frac{2j}{\pi\beta_\rho\rho}}\exp(-j\beta_\rho\rho) \quad \text{for } \beta_\rho\rho \gg 0, \tag{6}$$

where $\rho = |\bar{\rho} - \bar{\rho}'| \sim |\bar{\rho}'|$ for $|\bar{\rho}| \gg |\bar{\rho}'|$, where $|\bar{\rho}|$ and $|\bar{\rho}'|$ are the vectors (in the x–y plane) of the observation point and the source, respectively. In the phase term in Eq. (6),

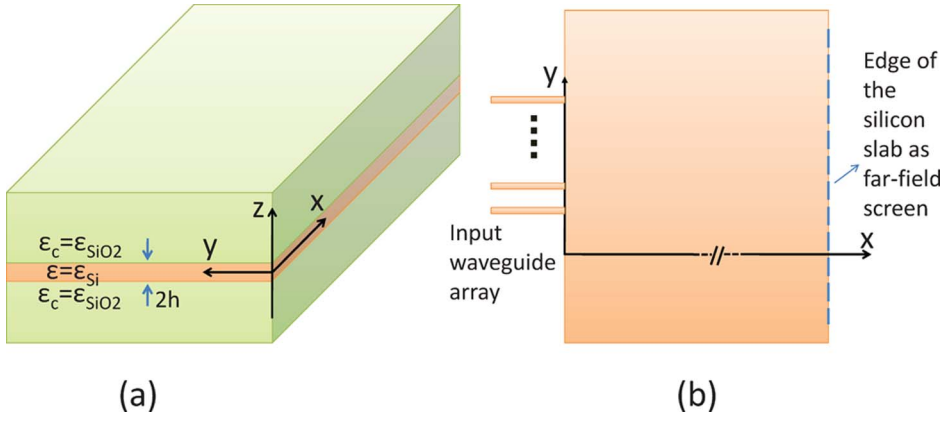

Fig. 1. (Color online) (a) Geometry of the silicon slab waveguide. (b) Schematic of the waveguide array connected to a large slab waveguide.

$$\rho = |\bar{\rho} - \bar{\rho}'| \sim |\bar{\rho}| - |\bar{\rho}'|\cos(\varphi - \varphi') + \frac{|\bar{\rho}'|^2}{2|\bar{\rho}|}$$
$$\sim |\bar{\rho}| - |\bar{\rho}'|\cos(\varphi - \varphi') \quad \text{for } \beta_\rho \frac{|\bar{\rho}'|^2}{2|\bar{\rho}|} \ll 1. \quad (7)$$

Therefore, the conditions to approximate the Green's function with a cylindrical wave in the far field are similar to those applied to spherical waves in 3D (free-space radiation) [8]:

1. $\beta_\rho \rho \gg 0$, or the effective wavelength should be much smaller than the observation distance;
2. $|\bar{\rho}| \gg |\bar{\rho}'|$, or the whole scattering object size (or the array size) should be much smaller than the observation distance; and
3. $\beta_\rho \frac{|\bar{\rho}'|^2}{2|\bar{\rho}|} \ll 1$ for the phase condition.

Of course, there are relevant differences with far-field radiation in free space: in this "flatland" far-field radiation, the local field radiated by a point source appears to be a slab (TE) mode, for which the magnetic field and propagation direction are not orthogonal. In other words, the far field is not a TEM wave, for which $\beta^2 = \omega^2\mu\varepsilon$. This is the main difference between 2D and 3D far-field radiation. In 2D, the polarization inherently depends on the level of confinement in the third (z) direction. Without a lack of generality, let us consider an observation point in the far field near the x axis ($y \ll x, |z| < h$). We can represent the propagating mode as a transmission-line mode as in [9]. The transmission-line (per unit length) voltages and currents are defined as $V = E_y|_{z=0}$ and $I = -H_z|_{z=0}$, which satisfy the standard transmission-line equations:

$$\frac{dV}{dx} = \left.\frac{\partial E_y}{\partial x}\right|_{z=0} = \left. -j\omega\mu H_z\right|_{z=0} = j\omega\mu I$$
$$\frac{dI}{dx} = -\left.\frac{\partial H_z}{\partial x}\right|_{z=0} = \left. j\omega\varepsilon E_y\right|_{z=0} - \left.\frac{\partial H_x}{\partial z}\right|_{z=0} = j\omega\varepsilon_{\text{eff}} V,$$

where

$$\varepsilon_{\text{eff}} = \varepsilon - \frac{\left.\frac{\partial H_x}{\partial z}\right|_{z=0}}{\left. j\omega\varepsilon E_y\right|_{z=0}}. \quad (8)$$

Thus, the effective permittivity of the mode is modified by presence of a longitudinal component of magnetic field H_x. The dispersion relation for the modes in the far field is compactly written in analogy with the regular free-space radiation:

$$\beta_\rho^2 = \omega^2\mu\varepsilon_{\text{eff}}. \quad (9)$$

In other words, within this framework, it is possible to treat the radiation from arbitrary point sources within the slab (2D) as one of the point sources in free space (3D), by simply considering an effective form of permittivity as defined in Eq. (8), similar to the concept of "flatland optics" [3].

Note that the definition of point source in the form of an impressed field given above lets us directly derive the field radiated from a waveguide interface into the slab region. In Fig. 1(b), at $x = 0$, where the array waveguides are connected to the slab waveguide, the waveguides' facets may be treated as collections of 2D point sources defined above, and thus, following the previous theoretical formulation, the overall radiated field inside the slab may be described as the one produced by an OPA. In particular, on the plane $x = 0$, the field may be calculated as

$$\sum_{n=1}^{N} \int_{-W_e/2}^{W_e/2} \frac{jA_n}{4\pi} \exp(-j\phi_n) H_0^{(2)}\left(\omega\sqrt{\mu\varepsilon_{\text{eff}}}\left|\bar{\rho} - \bar{d}_n - y\right|\right) \mathrm{d}y, \quad (10)$$

where N is the number of array elements, A_n is the field amplitude of the nth array waveguide, W_e is the effective width of a waveguide, including the penetration depth due to the Goos–Hänchen shift, $\bar{d}_n$ is the position (center) of the array elements, and φ_n is the input phase of the nth array waveguide. Also, ε_{eff} is the effective permittivity defined in Eq. (8). This formula can be simplified as shown in Eq. (7) in the far-field zone.

3. Experimental Observation of the 2D Far Field

In order to validate our theoretical results, we have designed and fabricated a three-element phased array fed by 1 × 3 MMI couplers. A schematic of a 1 × 3 MMI coupler is shown in Fig. 2. The input and output access waveguide widths are designed to be wide enough to ensure nearly ideal self-imaging behavior [10]. The MMI output waveguides' phase values are given as $\theta_q = \frac{N-1-4q^2}{4N}\pi$ [11–13], where N is the number of the MMI output ($N = 3$) and q is the port number, as shown in Fig. 2. For 1 × 3 MMIs, the middle output waveguide has a 60° phase lead compared to the two side ones. The MMI output waveguide widths are tapered at the end to 500 nm for single mode operation. Figure 2(b) shows the MMI coupler simulations by the vectorial eigenmode expansion simulator in FIMMPROP. The variations of the output uniformity and insertion loss are shown as a function of the MMI length are shown in Fig. 2(c).

The MMIs are fabricated on a silicon-on-insulator substrate with a 3 μm buried oxide layer. The silicon nanomembrane thickness $2h = 230$ nm. The MMIs are patterned using electron beam lithography, followed by reactive ion etching, lift-off pattern inversion, and plasma-enhanced chemical vapor deposition of a 1 μm thick silicon dioxide film for the top cladding. SEM pictures of the fabricated MMIs are shown in Fig. 3.

The MMI outputs are connected to a 2 cm wide and 1 cm long silicon slab waveguide. Using Eq. (7) for $\beta_\rho = 11.8\frac{\text{rad}}{\mu\text{m}}$, $|\bar{\rho}'| \le 9.3\,\mu$m, and $|\bar{\rho}'| \approx 10,000\,\mu$m, we know that the silicon slab waveguide is long enough

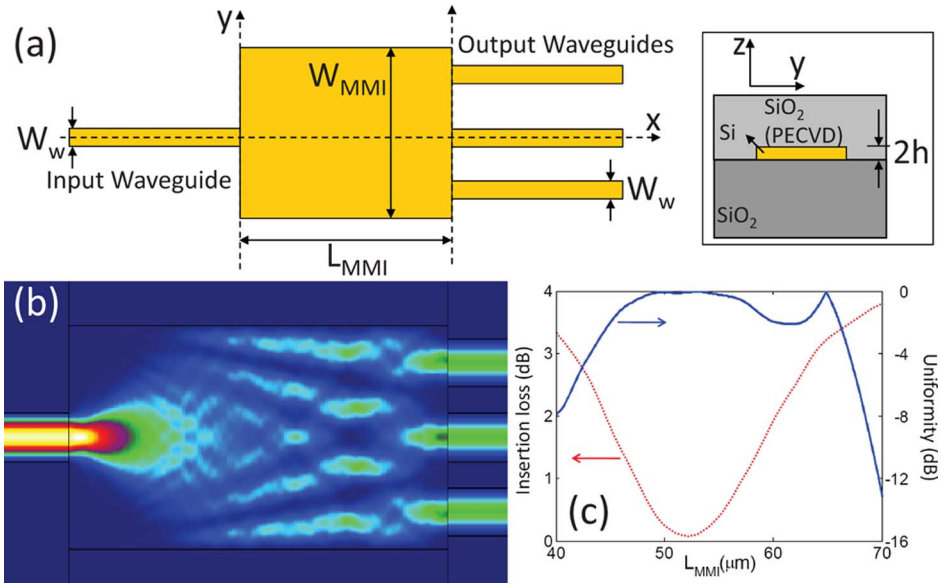

Fig. 2. (Color online) (a) Schematic of the 1×3 MMI used for the far-field test. The inset shows the cross section of the waveguiding structure. Access waveguide width, $W_w = 2\,\mu$m; MMI width, $W_{\mathrm{MMI}} = 9.3\,\mu$m; MMI length, $L_{\mathrm{MMI}} = 52.5\,\mu$m; MMI thickness, $2h = 0.23\,\mu$m. (b) Eigenmode-decomposition-based simulation of the designed 1×3 MMI. (c) Calculated output uniformity and insertion loss of the designed MMI.

for the far-field conditions to be satisfied. The resulting far-field beam is detectable at the exterior edge of the silicon nanomembrane. The silicon nanomembrane is etched away from the chip edge. This separates the background noise from the light coupled into the silicon substrate. The transverse-electric (TE) field from an external cavity tunable laser source is coupled into the input waveguides through a tapered and focused polarization maintaining fiber. A CCD camera captures top-down images of the scattered light at the etched silicon nanomembrane, as shown in Fig. 4.

Figure 5 demonstrates the observed 2D far field and compares it with the theoretical far-field expression given by Eq. (10). The excellent agreement between the

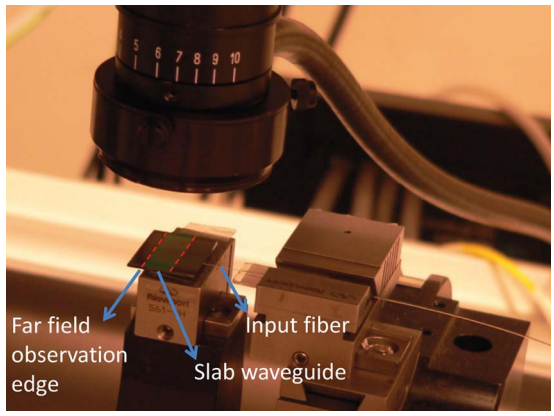

Fig. 4. (Color online) Optical test setup. The slab waveguide region on the chip is 8.0 mm long and is indicated by dashed lines.

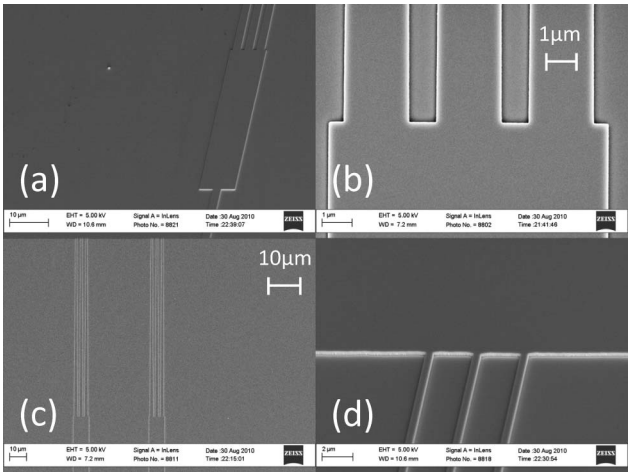

Fig. 3. (Color online) SEM images of (a) 1×3 MMI coupler, (b) 1×3 MMI coupler output, (c) output waveguides' width tapers, and (d) MMI output connections to the slab waveguide.

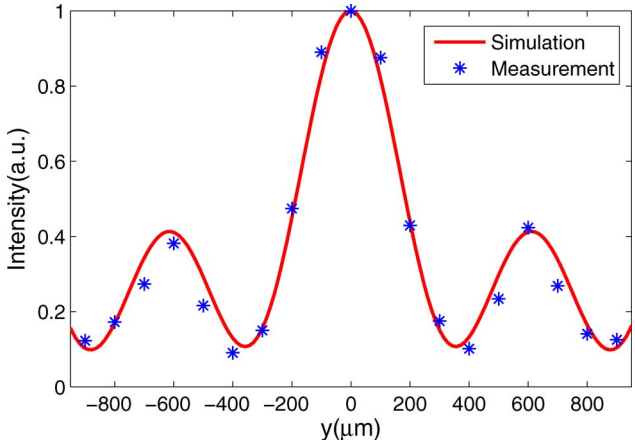

Fig. 5. (Color online) Two-dimensional far-field pattern of a 1×3 MMI with $3.1\,\mu$m separation between the output waveguides.

theoretical calculations and experimental results suggests that this formula, and also the experimental setup shown in Fig. 4, may be used to directly model and characterize radiation problems that involve 2D confined propagation. Also, Eq. (10) represents a solid design tool to tailor the phase of the different radiating elements on chip to synthesize the desired 2D far-field pattern.

4. Conclusions

We have presented here far-field modeling of 2D propagation in slab waveguides. The far-field conditions and field formulations have been derived. In order to experimentally observe the 2D far-field pattern, we have fabricated a 1×3 MMI coupler on a silicon nanomembrane. The MMI outputs are connected to a slab silicon waveguide, and the far field is observed at the edge of the silicon slab. These results may be used in the design and fabrication of OPA-based optical switches in integrated photonics, such as in Ref. [1].

Appendix A

We derive here an integral representation of the 2D Hankel function of use to derive Eq. (4) above. We know that [4]

$$H_0^{(2)}(\beta_\rho \rho, \phi) = \frac{1}{\pi} \int_{\pi/2-j\infty}^{3\pi/2+j\infty} \exp[j\beta_\rho \rho \cos(\zeta - \varphi)] \mathrm{d}\zeta.$$

One can write

$$\begin{aligned} H_0^{(2)}(\beta_\rho \rho, \varphi) &= \frac{1}{\pi} \int_{0-j\infty}^{\pi+j\infty} \exp[-j\beta_\rho \rho \sin(\zeta - \varphi)] \mathrm{d}\zeta \\ &= \frac{1}{\pi} \int_{0-j\infty}^{\pi+j\infty} \exp[-j\beta_\rho \rho \sin(\zeta)\cos(\varphi)] \\ &\quad \times \exp[j\beta_\rho \rho \cos(\zeta)\sin(\varphi)] \mathrm{d}\zeta \\ &= \frac{1}{\pi} \int_{0-j\infty}^{\pi+j\infty} \exp[-j\beta_\rho x \sin(\zeta)] \exp[j\beta_\rho y \cos(\zeta)] \mathrm{d}\zeta. \end{aligned}$$

By changing the variables, one can show

$$H_0^{(2)}(\beta_\rho \rho, \varphi) = \frac{1}{\pi} \int_{\varsigma=0-j\infty}^{\zeta=\pi+j\infty} \exp[-j\beta_\rho x \sin(\zeta)] \times \exp[j\beta_\rho y \cos(\zeta)] \frac{1}{\sqrt{\beta_\rho^2 - \beta_x^2}} \mathrm{d}\beta_x,$$

because

$$\begin{aligned} &\pi < \xi < \pi + j\infty \rightarrow -j\infty < \beta_x < 0j \quad \text{and} \quad \beta_\rho < \beta_y < \infty, \\ &\pi/2 < \xi < \pi \rightarrow 0 < \beta_x < \beta_\rho \quad \text{and} \quad 0 < \beta_y < \beta_\rho, \\ &0 < \xi < \pi/2 \rightarrow 0 < \beta_x < \beta_\rho \quad \text{and} \quad -\beta_\rho < \beta_y < 0, \\ &-j\infty < \xi < 0 \rightarrow -j\infty < \beta_x < 0j \quad \text{and} \quad -\infty < \beta_y < -\beta_\rho. \end{aligned}$$

Thus

$$H_0^{(2)}(\beta_\rho \rho, \varphi) = \frac{1}{\pi} \int_{\beta_y=-\infty}^{\beta_y=\infty} \exp[-j\beta_x x] \times \exp[j\beta_y y] \frac{1}{\sqrt{\beta_\rho^2 - \beta_x^2}} \mathrm{d}\beta_x.$$

Therefore, we can conclude

$$\int_{-\infty}^{\infty} \frac{1}{\beta_y} \exp(-j\beta_x x) \exp(-j\beta_y y) \mathrm{d}\beta_x = \pi H_0^{(2)}(\beta_\rho \rho).$$

References

1. M. Jarrahi, R. F. W. Pease, D. A. B. Miller, and T. H. Lee, "Optical spatial quantization for higher performance analog-to-digital conversion," IEEE Trans. Microw. Theory Tech. **56**, 2143–2150 (2008).
2. R. Zia and M. L. Brongersma, "Surface plasmon polariton analogue to Young's double-slit experiment," Nat. Nanotechnol. **2**, 426–429. (2007).
3. A. W. Lohmann, A. Pe'er, D. Wang, and A. A. Friesem, "Flatland optics: fundamentals," J. Opt. Soc. Am. A **17**, 1755–1762 (2000).
4. A. W. Lohmann, D. Wang, A. Pe'er, and A. A. Friesem, "Flatland optics. II. basic experiments," J. Opt. Soc. Am. A **18**, 1056–1061 (2001).
5. A. W. Lohmann, A. Pe'er, D. Wang, and A. A. Friesem, "Flatland optics. III. Achromatic diffraction," J. Opt. Soc. Am. A **18**, 2095–2097.
6. A. Sommerfeld, *Partial Differential Equations in Physics* (Academic, 1949).
7. M. Abramowitz and I. A. Stegun, *Handbook of Mathematical Functions with Formulas, Graphs, and Mathematical Tables* (Dover, 1972).
8. C. A. Balanis, *Advanced Engineering Electromagnetics* (Wiley, 1989).
9. A. Alù and N. Engheta, "Optical nanotransmission lines: synthesis of planar left-handed metamaterials in the infrared and visible regimes," J. Opt. Soc. Am. B **23**, 571–583 (2006).
10. A. Hosseini, H. Subbaraman, D. Kwong, Y. Zhang, and R. T. Chen, "Optimum access waveguide width for $1 \times N$ multimode interference couplers on silicon nanomembrane," Opt. Lett. **35**, 2864–2866 (2010).
11. E. R. Thoen, L. A. Molter, and J. P. Donnelly, "Exact modal analysis and optimization of $N \times N \times 1$ cascaded waveguide structures with multimode guiding sections," IEEE J. Quantum Electron. **33**, 1299–1307 (1997).
12. J. M. Heaton and R. M. Jenkins, "General matrix theory of self-imaging in multimode interference (MMI) couplers," IEEE Photon. Technol. Lett. **11**, 212–214 (1999).
13. A. Hosseini, D. N. Kwong, C.-Y. Lin, B. S. Lee, and R. T. Chen, "Output formulation for symmetrically excited one-to-N multimode interference coupler," IEEE J. Sel. Top. Quant. Electron. **6**, 53–60 (2010).